SEEDING to enable sensitive electrochemical detection of biomarkers in undiluted biological samples

Jonathan Sabaté del Río
  https://orcid.org/0000-0002-3295-5851

Hyun-Kyung Woo
  Center for Soft and Living Matter, Institute for Basic Science (IBS), Department of Biomedical
Engineering, Ulsan National Institute of Science and Technology

Juhee Park
  IBS   https://orcid.org/0000-0002-8109-6387

Hong Koo Ha
  Pusan National University Hospital, Pusan National University School of Medicine

Jae-Ryong Kim
  4Department of Biochemistry and Molecular Biology, Smart-aging Convergence Research Center,
College of Medicine, Yeungnam University

Yoon-Kyoung Cho (✉ ykcho@unist.ac.kr)
  IBS   https://orcid.org/0000-0001-6423-1834

Article

SEEDING to enable sensitive electrochemical detection of biomarkers in undiluted biological samples

Jonathan Sabaté del Río[1], Hyun-Kyung Woo[1,2], Juhee Park[1], Hong Koo Ha[3], Jae-Ryong Kim[4], Yoon-Kyoung Cho[1,2*]

[1]Center for Soft and Living Matter, Institute for Basic Science (IBS), Ulsan, 44919 Republic of Korea; [2]Department of Biomedical Engineering, Ulsan National Institute of Science and Technology (UNIST), Ulsan, 44919 Republic of Korea; [3]Department of Urology, Pusan National University Hospital, Pusan National University School of Medicine, Busan 49241, Republic of Korea; [4]Department of Biochemistry and Molecular Biology, Smart-aging Convergence Research Center, College of Medicine, Yeungnam University, Daegu 42415, Republic of Korea;

*Correspondence to: ykcho@unist.ac.kr (Y.-K.C.)

Abstract

The interface between an electrode and a liquid plays a critical role in the overall performance of electrochemical biosensors. Surface morphology and roughness affect key parameters, such as the active area, diffusion profiles, and apparent electron transfer kinetics, whereas porosity may hinder the diffusion of fouling proteins. However, there is no simple and rapid method compatible with photolithographic electrodes to generate both nanostructured and porous surfaces. Herein, we demonstrate the interplay between the preferential etching of chloride and surfactant-assisted anisotropic gold reduction to create homogeneous, nanostructured, and nanoporous substrates on photolithographic gold electrodes within a minute and without using templates. We coined this process, SEEDING, that is, Surfactant-based Electrochemical Etch-Deposit Interplay for Nanostructure/Nanopore Growth. SEEDING on electrodes enhanced the sensitivity and anti-biofouling capabilities, enabling direct analysis of small molecules, proteins, and cancer-derived extracellular vesicles in complex biological fluids such as undiluted plasma and urine samples.

Compact and affordable analytical tools that can rapidly perform sensitive, selective, and multiplexed detection of biological markers are essential for disease diagnostics and implantable sensors. Electrochemical readout platforms present an affordable and sensitive approach, along with miniaturised and simple instrumentation, promoting the fabrication and generalisation of point-of-care medical devices. However, the application of biosensors in diagnostic platforms still faces limitations when measuring relevant clinical samples typically comprising complex biological fluids, such as plasma, because of surface inactivation and sensitivity loss from non-specific adsorption and accumulation of sample proteins.

Sampling and molecular analysis of human biofluids hold great promise for cancer diagnosis, prognosis, and treatment response assessment[1]. Extracellular vesicles (EVs) secreted by all cells are present in large numbers in nearly all body fluids and contain invaluable protein and genetic information, thereby playing an essential role in various physiological and pathological processes[2]. Therefore, EVs are potential biomarker candidates for liquid biopsy analyses; for instance, tumour-derived EVs (tEVs) are critically related to tumour progression, metastatic niche formation, and immune evasion[3, 4]. However, despite their large concentration in plasma, tEVs still represent a minority of all EVs in the body. Additionally, EVs still represent a minor sub-population of all circulating particles in the blood and are outnumbered by lipoproteins by up to six orders of magnitude[5]. Therefore, conventional analysis methods typically require EVs separation, concentration, and purification steps which significantly affecting analysis time and sample volume requirement[6].

Studies on the detection of tEVs from plasma or serum have mainly been achieved using optical methods[7, 8]. However, the high sensitivity required, along with the large concentration of contaminants in clinical samples, impose a compromise between

62 sensitivity and selectivity in electrochemical biosensors[9]. A sensitive electrochemical

63 biosensor with anti-biofouling capabilities may address these requirements providing

64 a high-throughput tool for tEV diagnostics of small-volume liquid biopsies.

65   The sensitivity of electrochemical biosensors can be enhanced by increasing their

66 surface area[10], thereby lowering their limit of detection[11] and yielding enhanced

67 apparent electron transfer kinetics and improved bioreceptor functionalisation yield[12].

68 However, a large available surface area also increases biofouling, the non-specific

69 adsorption of sample proteins and molecules, with a subsequent decrease in

70 sensitivity. In this regard, the formation of nanoporous structures may be beneficial for

71 limiting the diffusion of undesired fouling proteins[9, 13-15], although the same principle

72 limits the detection of desired analytes[16, 17].

73   In this study, we present SEEDING, that is, Surfactant-based Electrochemical

74 Etch-Deposit Interplay for Nanostructure/Nanopore Growth, a method to fabricate gold

75 electrodes that combine nanostructured surfaces and nanoporous substrates,

76 achieving the benefits of both strategies, namely, large available electroactive areas

77 and limited diffusion and adsorption of non-specific proteins. As proof of concept, we

78 designed selective biosensors to detect electroactive molecules, an inflammatory

79 marker interleukin 6 (IL6) protein, and Epithelial Cell Adhesion Molecule

80 (EpCAM)[+]EVs from undiluted biological samples, such as cell culture media, blood

81 plasma, and urine. The process is a simple, cost-efficient, and rapid electrochemical

82 method that can be conducted on photolithographic chips for mass production of

83 disposable assay chips typically used in portable or handheld devices.

84

## SEEDING mechanism: Formation of nanostructured and nanoporous surfaces

Application of specific electric potentials to an electrode can transfer electrons from and to nearby molecules in solution, or atoms from the electrode, thereby changing the oxidation state of the species involved. For instance, we can electro-oxidise the surface of the electrode to etch materials and/or electrodeposit soluble materials on the electrode. By repeating this process, we can gradually transform a flat electrode into a nanostructured and nanoporous gold (NSG) electrode (**Fig. 1a**). Electrochemistry provides a convenient tool for controlling the kinetics and thermodynamics of these reactions. However, it is essential for this etch-deposit process to be anisotropic to create NSG electrodes. In other words, the interplay between the etch and deposit process must be balanced and exhibit spatial preference. Otherwise, each process would simply cancel each other, etching gold where it was deposited previously, leading to simple surface roughening[18].

To achieve controlled and directed growth, we designed the SEEDING method. We used a sodium chloride solution for electrooxidising and etching gold from a flat electrode and chloroauric acid and cetyltrimethylammonium (CTA$^+$) surfactant for preferential growth orientation during electroreduction. By quickly repeating these steps, we see that the anodic and cathodic currents, representing the oxidation and reduction of gold, increase over time reaching a stable current within a minute (**Fig. 1b, Supplementary Fig. 1**). This current is related with the available electroactive area, indicating growth of nanostructures, a process not observed using control solutions containing only one or two of the three components.

The fabricated NSG electrodes exhibited a distinctive dark homogeneous coloration on the surface (**Fig. 1c**). At the microscopic level, the original gold surface

110 comprised polycrystalline gold grains. Grain boundaries were preferential etching sites

111 that would create large crevasses and eventually act as nucleation points where gold

112 would be preferentially deposited. The deposits grow densely and eventually have a

113 coral reef shape with ~20 nm grain aggregates (**Fig. 1d**, **Supplementary Fig. 2**)

114 spanning homogeneously across the entire electrode surface (**Supplementary Fig.**

115 **3**). The root-mean-square roughness measured by atomic force microscopy (AFM)

116 can reach values of 340 ± 90 nm for NSG *vs*. the flat gold (1.2 ± 0.3 nm) (**Fig. 1e**),

117 which leads to a hydrophobic character because of the extreme roughness (**Fig. 1f**).

118   If we conduct the same process by scanning the voltage on the electrode within a

119 potential window, the process can be analysed in more detail (**Fig. 2**). Initially, a

120 solution of CTA^+ in contact with a gold surface forms a compact and homogeneous

121 bilayer that passivates the electrode for direct reduction of gold (**Fig. 2-①**), and CTA^+

122 in solution aggregate in micelles that coordinate with free chloroauric acid[19]. However,

123 when poising the electrode at anodic potential, chloride can diffuse toward the gold

124 surface[20] generating compact chloride adatoms at preferential sites[21] (**Fig. 2-②**),

125 during which both CTA^+ and chloride adlayers are co-adsorbed on the electrode[22, 23].

126 When the onset potential for oxidation is reached, gold is etched with chloride (**Fig. 2-**

127 **③**), generating chloroauric acid in the process[21] following the reaction[24]:

128 $$Au + 4Cl^- \rightarrow AuCl_4^- + 3e^- \qquad E^0 = 1.002\,V \qquad (1)$$
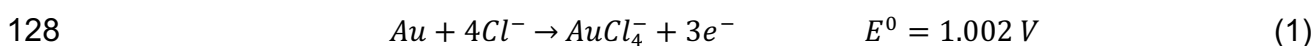
129   This process is anisotropic, preferentially etching away gold at specific step edges,

130 kinks, and vacancies, where the formation of chloride adlayers is more stable[21],

131 generating, in turn, more nucleation points for growing nanostructures. The freshly

132 dissolved chloroauric acid quickly coordinates with free micellar CTA^+ in solution,

133 preventing chloroauric acid from diffusing away from the surface. Switching the polarity

134 of the scan rate, we observe the micellar $CTA-AuCl_4$ being reduced and deposited on

135   the surface of the electrode at ~0.6 V (**Fig. 2-④**), an overpotential required because

136   of the formed CTA$^+$ layer on gold, following reaction (1) in reverse order.

137   Reduction of the CTA-AuCl$_4$ proceeds anisotropically, preferentially on the gold

138   facets where the CTA$^+$ layer is less dense, the surface energy is lower, and the edges

139   of the crystalline faces increase the curvature. Thus, access to micelles is easier,

140   increasing the reduction rate of gold species, promoting more efficient growth[25, 26] (**Fig.**

141   **2-④**). Iteration of this process yields the formation of increasingly large surfaces, so

142   the cathodic current at this step is more significant after each cycle (**Fig. 2** cyclic

143   voltammogram).

144

145   <u>Electrochemical and antifouling properties of NSG</u>

146   A method to calculate the gold surface area is the electrochemical oxidation of

147   gold followed by integrating the cathodic peak during electroreduction. Following this

148   method, the SEEDING process achieved a roughness factor >200 (**Fig. 3a**).

149   The oxidation/reduction of an equimolar electroactive couple, potassium

150   ferrocyanide and potassium ferricyanide, exhibits a reversible redox reaction with

151   diffusion-limited kinetics in both electrodes but with increased current densities for

152   NSG than flat gold electrodes (**Fig. 3b**) This is caused by the morphology of the

153   surface of the electrode, accounting for both the roughness[27, 28] and porosity[29], which

154   could enhance the apparent electrode kinetics and depend on the cumulative pore

155   volume and size[30]. At slow scan rates and in longer time-scale experiments, the

156   electrode kinetics are governed by larger diffusion layers. Therefore, the process is

157   diffusion-limited, and most of the electrodes present semi-infinite planar diffusion

158   layers similar to a flat electrode. However, at faster scan rates, where the diffusion

159   layers are smaller and become comparable to the size of the electrode nanostructures

160 and nanopores, the enhanced electrode kinetics arise from the morphology of the

161 electrodes (**Fig. 3c**).

162 The formation of oxide adlayers on polarised gold electrode surfaces exhibits

163 crystalline face selectivity, that is, the voltammetric oxidation peak has different energy

164 for each crystalline facet orientation Au{100} < Au{110} < Au{111}[31-33]. NSG electrodes

165 prepared at 1.20 V oxidating potential show an increase in Au{110} compared to

166 Au{100} and Au{111} (**Fig. 3d**). Grazing incidence X-ray diffraction on the NSG

167 electrodes revealed the expected peaks for polycrystalline gold indexed to diffraction

168 from the Au(111), Au(200), Au(220), and Au(311) planes of the face-centred cubic (fcc)

169 structure of metallic gold (JCPDS, card# 04-0784). The NSG surfaces exhibit an

170 increased peak intensity compared to the flat gold electrodes, which could be

171 explained by the increased thickness of the NSG electrode (**Fig. 3e**). The mean size

172 of the crystalline domain for NSG was 21 ± 4 nm (**Supplementary Table 1**),

173 comparable to the grain size observed with scanning electron microscopy (SEM) (**Fig.**

174 **1d**, **Supplementary Fig. 3**) but with different facet relative abundances

175 (**Supplementary Table 1**). The crystalline orientation of Au{110} was the most

176 abundant in both cases, flat gold and NSG, in agreement with previous

177 electrochemical measurements (**Fig. 3d**). However, the relative abundance of Au{100}

178 and Au{111} facet formation was larger in NSG than in flat gold (**Supplementary**

179 **Table 1**). Additionally, the relative abundance of Au{111} and Au{100} is small

180 compared to the abundant Au{110} peak, probably because the interatomic gold

181 distance of this facet opens a cavity large enough to accommodate CTA$^+$ cationic

182 heads[25].

183 To assess the anti-biofouling performance of the NSG electrodes, we compared

184 the electron charge transfer resistance (R_{ct}), that is, the resistance to transfer an

185   electric charge between the electrode and a diffusible redox molecule in different

186   media. Flat surfaces showed large adsorption of BSA increasing R_{ct} >4000% of their

187   original value, whereas NSG remained almost undisturbed during 20 h of exposure

188   (**Fig. 3f**). The same trend was observed in plasma, with the NSG displaying one order

189   of magnitude less R_{ct}. The anti-biofouling capability of NSG is attributed to the limited

190   diffusion of the biofouling proteins throughout the nanopore substrate[15], effectively

191   limiting absorption and preventing the blocking of available electroactive sites (**Fig.**

192   **3g**).

193

194   Applications of NSG electrodes for biosensing

195   We tested NSG electrodes for biosensing and diagnostic applications using

196   various analytes. First, we detected ferrocyanide, an electroactive redox molecule, to

197   understand the fundamental analytical parameters of these substrates. Then, we

198   designed an immunoaffinity biosensor functionalising the surface of the NSG electrode

199   with an appropriate bioreceptor for the detection of IL6, a soluble protein inflammatory

200   marker commonly found in plasma. A specially tuned detection strategy was used to

201   exploit the potential of our NSG electrodes while avoiding biofouling from the plasma.

202   Later, this detection strategy was translated to detect generic EVs through binding the

203   transmembrane proteins such as CD9 and CD81. Finally, we analysed a small cohort

204   of clinical samples from patients with prostate cancer, detecting minute concentrations

205   of tEVs from undiluted blood plasma[34].

206   The voltammetric detection of ferrocyanide (**Fig. 4a**) drives a redox reaction with

207   rapid electron transfer compared with the diffusion of species towards the surface. The

208   diffusion profile for this reaction on flat electrodes is planar, whereas on the irregular

209   surface of NSG, a radial contribution is responsible for the increased sensitivity from

210 6 to 14 $\mu A\ mm^{-2}\ mM^{-1}$ (**Fig. 4a**). However, at low concentrations, these species do not

211 have enough time to diffuse within the entire porous substrate before the reaction

212 occurs, and the limit of detection (LOD) is marginally improved by using NSG

213 electrodes (from 0.3 to 0.1 mM), which is in agreement with findings of previous

214 studies[16, 17].

215   Therefore, we designed a detection strategy for our biosensor based on the

216 formation of an electroactive adsorbate compound that precipitates on the surface of

217 the electrode during the detection process. In this scenario, the kinetics of the

218 detection (oxidation of the mediator) is limited by the electron transfer of the mediator

219 to the surface of the electrode, rather than its diffusion[16, 17]. This strategy was tested

220 using a selective antibody-functionalised NSG electrode biosensor to detect IL6. The

221 protein detection was conducted by an ELISA on the electrodes, generating an

222 electroactive precipitate at the end of the assay, which yielded a large current output

223 proportional to the concentration of IL6 (**Fig. 4b**). This allowed us to conduct more

224 sensitive measurements, achieving a 17-fold higher sensitivity with an LOD of 1 pg

225 mL^{-1} for NSG (*vs.* 31 pg mL^{-1} for flat electrodes) (**Fig. 4c**). Moreover, the critical feature

226 was the robustness of the biosensor when conducted the same measurements in

227 human plasma. Although the flat electrodes were completely passivated and detection

228 of IL6 was not possible, the NSG electrodes showed only an increase of the LOD from

229 1 to 10 pg mL^{-1}. Surfaces in contact with a biological sample, such as plasma, quickly

230 adsorb proteins that generate a passivating multilayer. Furthermore, this process is

231 typically enhanced in nanostructured surfaces because a larger surface area is

232 available. This is why enhancing the sensitivity of the assay by only increasing the

233 surface area with nanostructures is not beneficial. Instead, it yields an unexpectedly

234 low sensitivity with real samples. However, if the electrode also has a large

235 nanoporous structure beneath the surface, the diffusion of these contaminating

236 proteins into the sensing area and the passivation are limited[15].

237   By harnessing the anti-biofouling and ultrasensitive detection capabilities of this

238 strategy, we employed the NSG-based electrochemical biosensor to detect tEVs in

239 undiluted blood plasma, which are promising biomarker candidates for minimally

240 invasive cancer diagnostics. Here, we functionalised the NSG electrodes with anti-

241 CD9, an EV-associated biomarker, to capture EVs on the surface and then used

242 specific detection antibodies to investigate the presence of particular biomarkers on

243 the EV.

244   NSG biosensors could capture EVs from lymph node carcinoma of the prostate

245 (LNCaP) cell culture supernatant spiked human plasma and selectively detecting the

246 biomarkers. We detected CD9 and CD81 for total EV quantification and EpCAM, a

247 tumour-associated antigen, for tEV quantification (**Fig. 4d**). NSG biosensors allowed

248 us to detect total EVs and tEVs with high sensitivity in 5 µL of plasma, achieving a

249 LOD for total EVs (CD9$^+$EVs) of 60 vesicles µL^{-1} and tEVs (EpCAM$^+$EVs) of 300

250 vesicles µL^{-1}. For comparison, flat gold electrodes were electrically passivated during

251 the assay in plasma, and the ELISA required 50 µL of sample, achieving a LOD in

252 PBS of 700 vesicles µL^{-1} for total EVs and 8000 vesicles µL^{-1} for tEVs (**Supplementary.**

253 **Fig. 4a**).

254   To investigate whether NSG biosensors could be used to detect tEVs in clinical

255 samples, we analysed the concentration of CD9$^+$EVs and EpCAM$^+$EVs. EV signals in

256 urine samples were drawn from a small cohort (n = 10) that included patients with

257 prostate cancer (stages II, III, and IV), aged 54–82 years. Urine CD9$^+$EV levels were

258 not significantly higher in patients with prostate cancer than in healthy controls (**Fig.**

259 **4e**), whereas EpCAM$^+$EV levels were higher in patients with prostate cancer (p <

11

260   0.0001). Ultimately, we developed electrochemical biosensors that could operate in

261   complex biological fluids such as undiluted blood plasma. Accordingly, we tested the

262   blood plasma of a larger cohort (n = 18), which included patients with prostate cancer

263   (stages II, III, and IV), aged 66–82 years. EpCAM$^+$EV levels were significantly higher

264   in patients with prostate cancer than in healthy controls (**Fig. 4f**). Receiver operating

265   characteristic (ROC) curves indicated that EV detection using single associated

266   marker CD9$^+$EVs showed extensive overlap across the groups, with no discriminatory

267   power for classifying patients with cancer *vs.* healthy controls (**Fig. 4g**). Moreover,

268   ELISA detection of either CD9$^+$EVs or EpCAM$^+$EVs in the same clinical samples could

269   not discriminate between healthy and cancer donors (**Supplementary. Fig. 4b-c**).

270   Interestingly, EpCAM$^+$EV levels measured by NSG biosensors in plasma were

271   approximately 10 times higher than those in urine. However, both urine and plasma

272   EpCAM$^+$EV levels constituted good classifiers (AUC 0.91 and 0.90, respectively) for

273   differentiating patients with prostate cancer from healthy cases (**Fig. 4g**). Finally, the

274   serum PSA levels of all cancer cohorts (urine and plasma) differed widely, showing no

275   correlation with prostate cancer stage (*p* = 0.7454) or Gleason sum (*p* = 0.6940).

276   Therefore, these results indicated a correlation between circulating EpCAM$^+$EV levels

277   in both urine and plasma and the presence of prostate cancer. Notably, these clinical

278   samples were analysed directly with the NSG electrodes, without dilution or

279   preprocessing steps, suggesting the potential utility of this biosensing platform for

280   ultrasensitive detection of markers in complex matrices.

281

282   <u>Conclusions</u>

283   We developed SEEDING, a simple and fast (1 min) method to generate

284   nanostructured and nanoporous surfaces from photolithographic gold electrodes

285 without templates. The high electroactive area achieved on these surfaces increased

286 the sensitivity in bioassays because of the higher bioreceptor immobilisation yield.

287 Moreover, faster apparent electron transfer kinetics lead to amplification of the

288 electrochemical signals and porosity provided a size-exclusion mechanism that

289 prevented biofouling. This allowed direct exposure to biological fluids containing large

290 concentrations of contaminating proteins while maintaining high sensitivity.

291 Functionalising these surfaces with specific bioreceptors allowed the specific

292 detection of diffusible proteins or EVs in low-volume complex matrices. Because the

293 sensitivity of large surface electrodes is limited by the diffusion of species involved, we

294 took advantage of a transduction mechanism based on the precipitation of an

295 electrochemical mediator upon completion of the assay. Notably, ultrasensitive

296 detection of tEVs from small volumes of undiluted plasma and urine samples allowed

297 us to discriminate between healthy controls and patients with prostate cancer.

298 SEEDING offers key advantages over traditional nanostructuring or nanoporous

299 methods (**Supplementary Table 2**). Specifically, it is a relatively simple and fast

300 process that works on photolithographic chips and generates nanostructured and

301 nanoporous electrodes. The high sensitivity with anti-biofouling performance is a key

302 aspect for analysing low-concentration biomarkers in real samples. Therefore,

303 SEEDING may be used to develop quick, selective, sensitive, and miniaturised

304 diagnostics in biological samples.

305 # References

306 1.   Heitzer, E., Haque, I. S., Roberts, C. E. S. & Speicher, M. R. Current and future
307   perspectives of liquid biopsies in genomics-driven oncology. *Nat. Rev. Genet.* **20**, 71-
308   88 (2019).
309
310 2.   van Niel, G., D'Angelo, G. & Raposo, G. Shedding light on the cell biology of
311   extracellular vesicles. *Nat. Rev. Mol. Cell. Biol.* **19**, 213-228 (2018).
312

313   3.   Xu, R.*, et al.* Extracellular vesicles in cancer - implications for future improvements in
314   cancer care. *Nat. Rev. Clin. Oncol.* **15**, 617-638 (2018).
315
316   4.   Hoshino, A.*, et al.* Extracellular vesicle and particle biomarkers define multiple human
317   cancers. *Cell.* **182**, 1044-1061 e1018 (2020).
318
319   5.   Johnsen, K. B., Gudbergsson, J. M., Andresen, T. L. & Simonsen, J. B. What is the
320   blood concentration of extracellular vesicles? Implications for the use of extracellular
321   vesicles as blood-borne biomarkers of cancer. *Biochim. Biophys. Acta. Rev. Cancer.*
322   **1871**, 109-116 (2019).
323
324   6.   Li, W.*, et al.* Emerging nanotechnologies for liquid biopsy: The detection of circulating
325   tumor cells and extracellular vesicles. *Adv. Mater.* **31**, e1805344 (2019).
326
327   7.   Yoshioka, Y.*, et al.* Ultra-sensitive liquid biopsy of circulating extracellular vesicles
328   using ExoScreen. *Nat. Commun.* **5**, 3591 (2014).
329
330   8.   Liang, K.*, et al.* Nanoplasmonic quantification of tumor-derived extracellular vesicles in
331   plasma microsamples for diagnosis and treatment monitoring. *Nat. Biomed. Eng.* **1**,
332   (2017).
333
334   9.   Sabaté Del Río, J., Henry, O. Y. F., Jolly, P. & Ingber, D. E. An antifouling coating that
335   enables affinity-based electrochemical biosensing in complex biological fluids. *Nat.*
336   *Nanotechnol.* **14**, 1143–1149 (2019).
337
338   10.   Soleymani, L.*, et al.* Nanostructuring of patterned microelectrodes to enhance the
339   sensitivity of electrochemical nucleic acids detection. *Angew. Chem. Int. Edit.* **48**,
340   8457-8460 (2009).
341
342   11.   Soleymani, L., Fang, Z., Sargent, E. H. & Kelley, S. O. Programming the detection
343   limits of biosensors through controlled nanostructuring. *Nat. Nanotechnol.* **4**, 844
344   (2009).
345
346   12.   Bin, X., Sargent, E. H. & Kelley, S. O. Nanostructuring of sensors determines the
347   efficiency of biomolecular capture. *Anal. Chem.* **82**, 5928-5931 (2010).
348
349   13.   Daggumati, P., Kurtulus, O., Chapman, C. A., Dimlioglu, D. & Seker, E.
350   Microfabrication of nanoporous gold patterns for cell-material interaction studies. *J. Vis.*
351   *Exp.* e50678 (2013).
352
353   14.   Erlebacher, J., Aziz, M. J., Karma, A., Dimitrov, N. & Sieradzki, K. Evolution of
354   nanoporosity in dealloying. *Nature.* **410**, 450-453 (2001).
355
356   15.   Patel, J.*, et al.* Electrochemical properties of nanostructured porous gold electrodes in
357   biofouling solutions. *Anal. Chem.* **85**, 11610-11618 (2013).
358
359   16.   Daggumati, P., Matharu, Z., Wang, L. & Seker, E. Biofouling-resilient nanoporous gold
360   electrodes for DNA sensing. *Anal. Chem.* **87**, 8618-8622 (2015).
361
362   17.   Daggumati, P., Matharu, Z. & Seker, E. Effect of nanoporous gold thin film morphology
363   on electrochemical DNA sensing. *Anal. Chem.* **87**, 8149-8156 (2015).
364
365   18.   Arroyo-Currás, N., Scida, K., Ploense, K. L., Kippin, T. E. & Plaxco, K. W. High surface
366   area electrodes generated via electrochemical roughening improve the signaling of
367   electrochemical aptamer-based biosensors. *Anal. Chem.* **89**, 12185-12191 (2017).

19. Khan, Z., Singh, T., Hussain, J. I. & Hashmi, A. A. Au(III)–CTAB reduction by ascorbic acid: Preparation and characterization of gold nanoparticles. *Colloids Surf. B.* **104**, 11-17 (2013).

20. Ramírez-Rico, D. S. & Larios-Durán, E. R. Electrochemical study on electrodissolution of gold in acidic medium using chlorides as ligands. *J. Electrochem. Soc.* **164**, H994-H1002 (2017).

21. Ye, S., Ishibashi, C. & Uosaki, K. Anisotropic dissolution of an Au(111) electrode in perchloric acid solution containing chloride anion investigated by in situ STM - The important role of adsorbed chloride anion. *Langmuir.* **15**, 807-812 (1999).

22. Vivek, J. P. & Burgess, I. J. Quaternary ammonium bromide surfactant adsorption on low-index surfaces of gold. 1. Au(111). *Langmuir.* **28**, 5031-5039 (2012).

23. Vivek, J. P. & Burgess, I. J. Quaternary ammonium bromide surfactant adsorption on low-index surfaces of gold. 2. Au(100) and the role of crystallographic-dependent adsorption in the formation of anisotropic nanoparticles. *Langmuir.* **28**, 5040-5047 (2012).

24. Weast, R. C., Astle, M. J. & Beyer, W. H. *CRC Handbook of Chemistry and Physics*, vol. 84. (CRC Press LLC, Boca Raton, FL, 2004).

25. Chhatre, A., Thaokar, R. & Mehra, A. Formation of gold nanorods by seeded growth: mechanisms and modeling. *Cryst. Growth Des.* **18**, 3269-3282 (2018).

26. Meena, S. K., *et al.* The role of halide ions in the anisotropic growth of gold nanoparticles: a microscopic, atomistic perspective. *Phys. Chem. Chem. Phys.* **18**, 13246-13254 (2016).

27. Zuo, X., Xu, C. & Xin, H. Simulation of voltammogram on rough electrode. *Electrochim. Acta.* **42**, 2555-2558 (1997).

28. Menshykau, D., Streeter, I. & Compton, R. G. Influence of electrode roughness on cyclic voltammetry. *J. Phys. Chem. C.* **112**, 14428-14438 (2008).

29. Menshykau, D. & Compton, R. G. The influence of electrode porosity on diffusional cyclic voltammetry. *Electroanal.* **20**, 2387-2394 (2008).

30. Punckt, C., Pope, M. A. & Aksay, I. A. On the electrochemical response of porous functionalized graphene electrodes. *J. Phys. Chem. C.* **117**, 16076-16086 (2013).

31. Hersbach, T. J. P., Mints, V. A., Calle-Vallejo, F., Yanson, A. I. & Koper, M. T. M. Anisotropic etching of rhodium and gold as the onset of nanoparticle formation by cathodic corrosion. *Faraday Discuss.* **193**, 207-222 (2016).

32. Jeyabharathi, C., Ahrens, P., Hasse, U. & Scholz, F. Identification of low-index crystal planes of polycrystalline gold on the basis of electrochemical oxide layer formation. *J. Solid State Electrochem.* **20**, 3025-3031 (2016).

33. Hamelin, A. Cyclic voltammetry at gold single-crystal surfaces. Part 1. Behaviour at low-index faces. *J, Electroanal. Chem.* **407**, 1-11 (1996).

422   34.   Ni, J*., et al.* Role of the EpCAM (CD326) in prostate cancer metastasis and progression.
423   *Cancer Metastasis Rev.* **31**, 779-791 (2012).
424
425

Figures
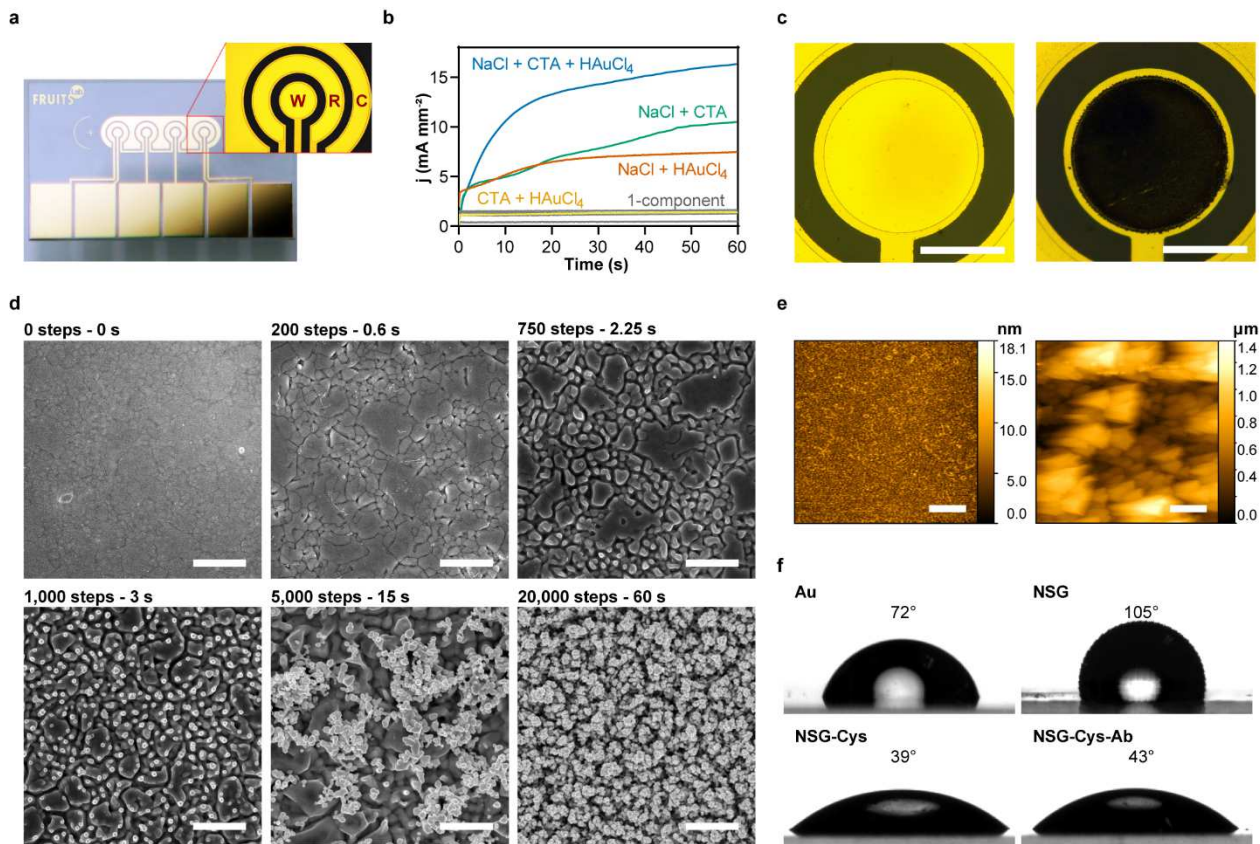
Fig. 1 | SEEDING of photolithographic flat gold electrodes. **a**, Photograph of a photolithographic gold electrode chip with four circular working gold electrodes, a common reference, and counter electrode. **b**, Typical chronoamperograms (only showing anodic currents) during the SEEDING process conducted in photolithographic gold electrodes in different control solutions (one-component controls are grayed out). **c**, Photographs of the photolithographic gold electrodes before (left) and after (right) the SEEDING process. Scale bar: 250 µm. **d**, Scanning electron micrographs of NSG electrodes conducted by chronoamperometry after a different number of step voltages. Scale bar: 1 µm. **e**, Atomic force microscopy topography of the photolithographic gold electrodes before (left) and after (right) the SEEDING process. Scale bar: 1 µm. **f**, Water

438   contact angle photographs for different surfaces and modifications (Au: bare gold, NSG:

439   nanostructured and nanoporous gold, NSG-Cys: NSG modified with L-cysteine, NSG-

440   Cys-Ab: NSG-Cys functionalised with antibodies).

441

442

Flat gold surface

Nanostructured gold surface
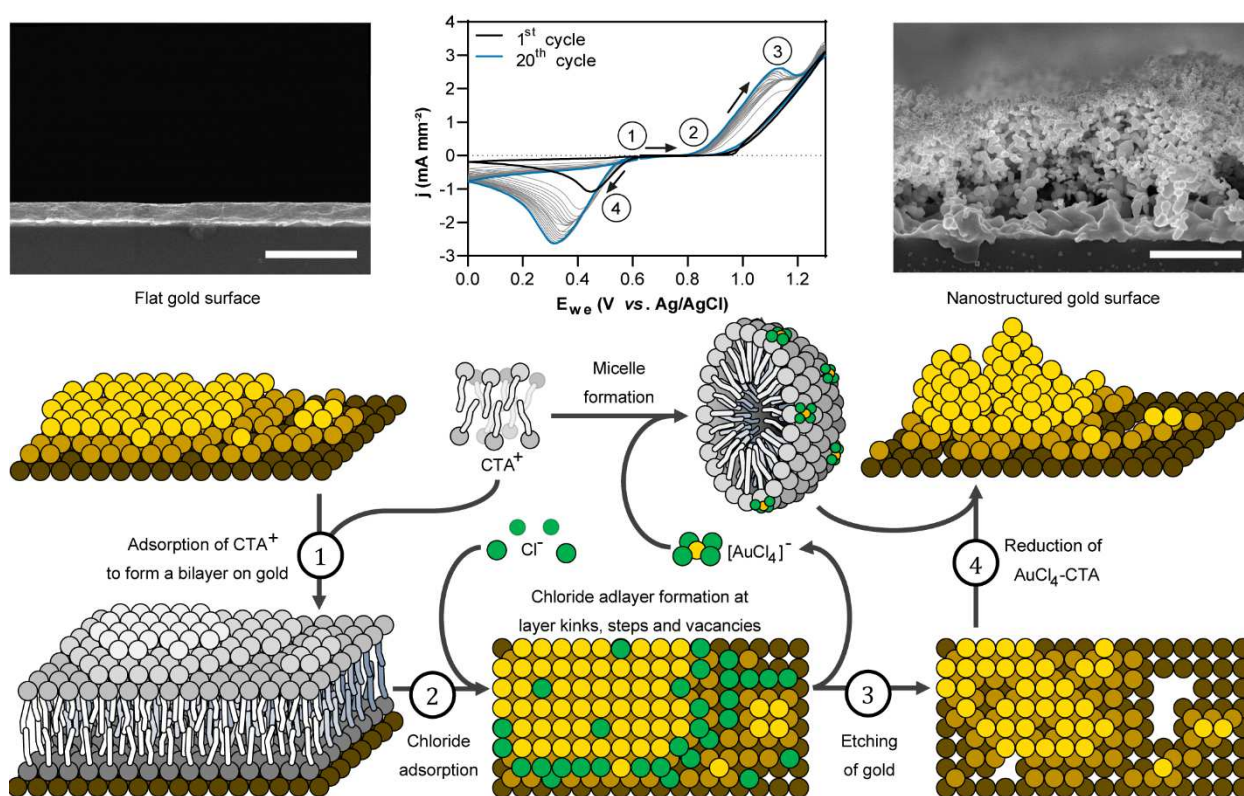
Fig. 2 | Schematic illustration of SEEDING. The SEEDING process is electrochemically conducted in the presence of chloride, CTA^+-based surfactant, and chloroauric acid. (black: first scan; grey: subsequent scans; blue: last scan). ①, Adsorption of CTA^+ takes place on gold, electrically passivating the surface of electrodes. Additionally, CTA^+ ions create micelles in the solution, which are loaded with negatively charged chloroauric acid. ②, Electrochemically driven adsorption of chlorine adlayers on gold step layers occurs, and ③, etching of the surface finally occurs, generating chloroauric acid. ④, Electrochemically driven adsorption and reduction of gold-laden CTA^+ micelles. The scanning electron micrographs show the cross-section of a

453   photolithographic gold electrode before (left) and after (right) conducted the SEEDING

454   process. Scale bar: 1 µm.

455
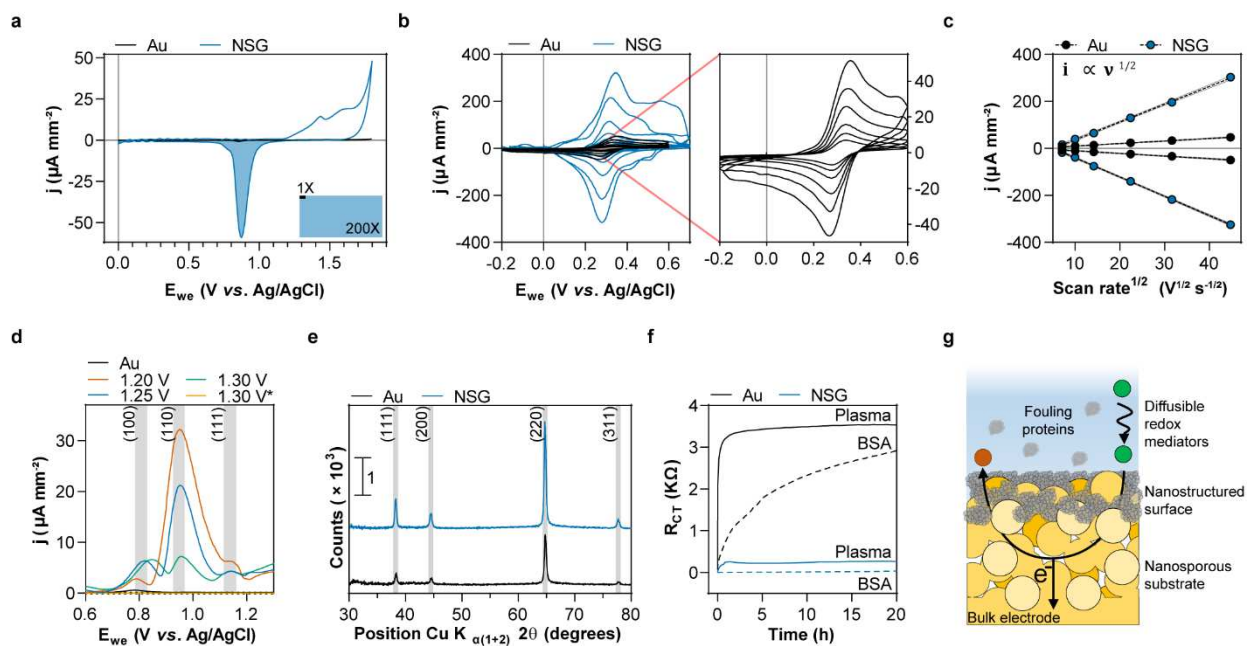
Fig. 3 | Electrochemical and antifouling properties of nanostructured and nanoporous gold. **a,** Cyclic voltammogram of a flat (black) and an NSG electrode (blue) in acidic media (inset: schematic area enhancement). **b**, Cyclic voltammogram showing oxidation and reduction peaks of an equimolar solution of 2.5 mM ferri/ferrocyanide at various scan rates for a flat gold electrode (black) and an NSG electrode (blue). The right side plot is a magnified voltammogram of the flat electrode. **c**, Randles-Sevçik plot of oxidation and reduction peak currents (i_p) (circles) *vs.* the square root of the scan rate (extracted from the voltammograms in b) (n = 4 independent electrodes). Error bars represent the standard deviation of the mean. **d**, Square-wave scan voltammograms of NSG electrodes prepared by chronoamperometry at different oxidation potentials *vs.* a flat electrode as a control. (*no reduction step) **e**, Grazing incidence X-ray diffraction spectrogram of an NSG electr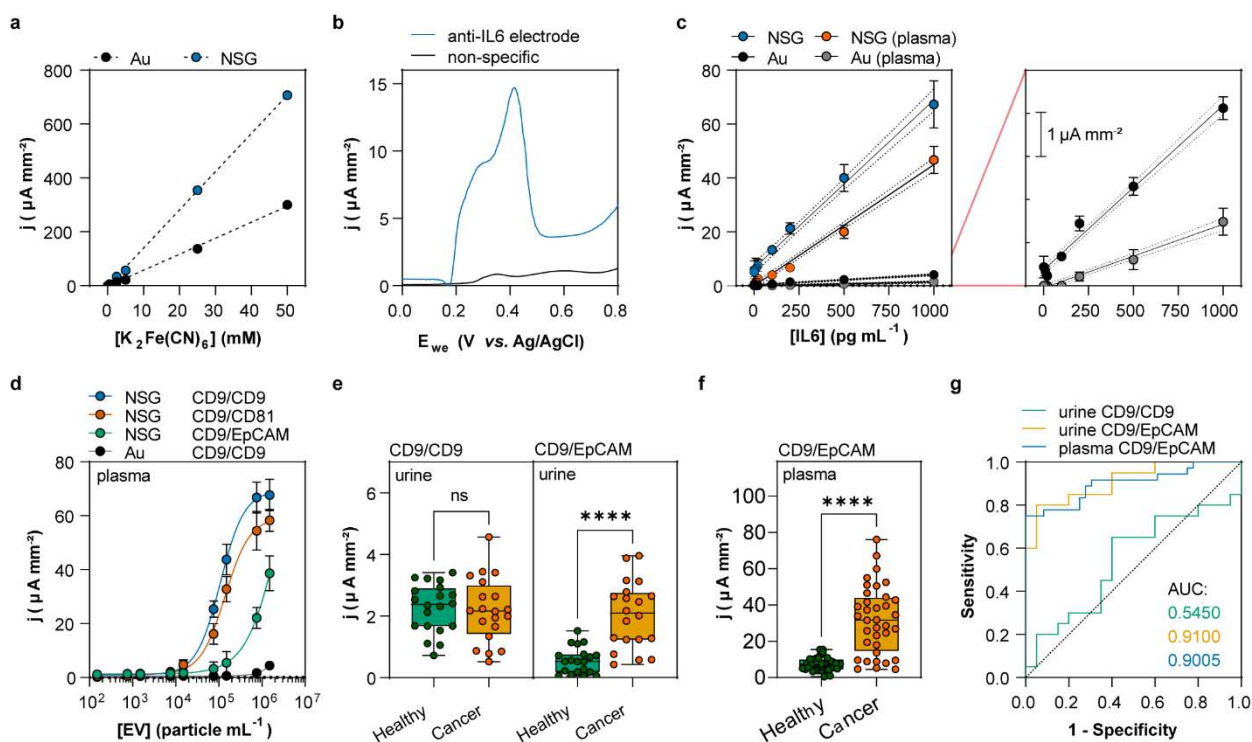ode *vs.* a flat gold electrode. **f**, Plot of charge transfer resistance change over time for a flat electrode (black lines) *vs.* an NSG electrode (blue lines) in BSA 1% or human plasma (dashed lines). **g**, Schematic illustration of fouling

471   mechanism on a porous electrode with pore size diameters smaller than the fouling

472   proteins.

473

Fig. 4 | Application of nanostructured porous gold electrodes for analysis. **a**, Calibration plot representing peak current densities *vs.* concentration for the electrochemical detection of ferrocyanide on a flat electrode (black circles) *vs.* NSG electrodes (blue circles) (n = 4 independent electrodes). Error bars represent the standard deviation of the mean. **b**, Typical voltammetric oxidation peaks of precipitated electroactive reagent corresponding to a detection immunoassay on the NSG electrode chips. **c**, Calibration plot representing oxidation peak current (circles) recorded on NSG electrodes *vs.* flat electrodes (magnified on the right side) at different concentrations of IL6 spiked in PBS or human plasma (n = 4 independent electrodes). Error bars represent the standard deviation of the mean. **d**, Calibration plot for CD9+, CD81+ or EpCAM+ on CD9-captured EV, representing peak current densities (circles) *vs.* particle concentration using NSG or flat electrodes (n = 4 independent electrodes). Error bars represent the standard deviation of the mean. **e**, Analysis of clinical urine samples using NSG

488   biosensors showing current density values (circles) with different assay schemes,

489   detection of CD9$^+$ or EpCAM$^+$ on CD9-captured EV (n = 20 for each box, five biological

490   samples with four technical replicates for each). The boxes extend from the 25th to 75th

491   percentiles, the middle line is the median, and the whiskers extend from min to max values.

492   **f**, Electrochemical current density values (circles) for different clinical human plasma

493   samples from healthy and patients with cancer regarding the detection of EpCAM$^+$ on

494   CD9-captured EVs (n = 36 for each box, nine biological samples with four technical

495   replicates for each). The boxes extend from the 25th to 75th percentiles, the middle line is

496   the median, and the whiskers extend from min to max values. **g**, ROC curves showing

497   the classification ability (healthy, cancer) for the three employed assays using either urine

498   or plasma clinical samples.

Methods

Fabrication and preparation of the planar electrodes

Planar electrodes were fabricated in a cleanroom using standard lithography processes on 4-inch soda-lime glass wafers (Product #1631, University wafers), generating 44 chips (1.5 × 0.9 mm) containing four working electrodes. First, 20 nm of titanium and 400 nm of gold were deposited by e-beam evaporation (FC-2000, Temescal). Following spin coating (4000 rpm, 500 rpm s^{-1}, 1 min) of a 1.3 µm-thick photoresist (AZ® 5214 E, MicroChemicals GmbH), and evaporation of the solvent on a hot plate (90 s at 105 °C), the wafer was exposed in a mask aligner (MA/BA6, SUSS MicroTec Korea Co. Ltd.) (h-line 405 nm, 90 mJ cm^{-2}) using a Mylar mask (Advance Reproductions, USA) attached to a blank glass. After developing the photoresist (AZ® MIF 326, MicroChemicals GmbH) to transfer the pattern, the exposed gold layer was etched with a gold etchant (cat# 651818-500ML, Sigma-Aldrich) for 1 min, and the titanium layer was stripped with a buffered oxide etchant (BOE 7:1, MicroChemicals GmbH) for 40 s. The remaining positive photoresist was removed in isopropyl alcohol, and a 2 µm-thick photoresist (SU-8 2002, K1 Solution) spin-coated on the wafer (3000 rpm, 500 rpm s^{-1}, 1 min). Following a pre-baking step of the negative photoresist (1.5 min at 65 °C and 3 min at 95 °C), the wafers were exposed in a mask aligner (i-line 365 nm, 120 mJ cm^{-2}) and quickly post-baked (1.5 min at 65 °C and 1.5 min at 95 °C) before developing the photoresist (SU-8 developer, K1 Solution) to open up the electric contacts and limit the sensing area on the electrodes. Finally, the chip was rinsed with isopropyl alcohol, and the negative photoresist was further cured in a hard-bake step (3 h at 180 °C). A protective layer of positive photoresist was spin-coated to protect the chips during dicing and keep

522 them clean during storage. Before use, the chips were rinsed in acetone and cleaned in

523 O_2 plasma (Cute, Femto Science) at 0.5 mbar and 50 mW for 2 min.

Preparation of gold rod electrodes

525 Gold rod electrodes (Φ = 2 mm, cat# CHI101, Qrins) were prepared before use with

526 a polishing kit (cat# CHI120, Qrins) by consecutively polishing their surfaces against

527 alumina slurries of different sizes on a polishing pad. First, we used a 1 µm slurry on a

528 CarbiMet^{TM} disk, a 0.3 µm slurry on a nylon pad, and finally, a 0.05 µm slurry on a

529 microcloth pad using an "8"-shaped motion for approximately 30 s, and sonicating the

530 electrode in a water bath (3510, Branson) for 1 min after each polishing step.

Preparation of SEEDING solution

532 The solution for SEEDING electrodes was prepared by dissolving 36 mg of CTAC

533 (TCI, cat# H0082, lot# 4LL50-MN) per millilitre of a 222 mM sodium chloride stock solution.

534 Then, 1/9 of the volume was added as chloroauric acid 10 mM (stock stored in the dark

535 at 4 °C) to obtain a final concentration of CTAC 100 mM, NaCl 200 mM, and $HAuCl_4$ 1

536 mM. This solution was stable at room temperature (25 ºC) when stored in the dark.

537 Preparation using CTAB (Sigma-Aldrich, cat# 52365-50G, lot# BCBT1510) generated

538 similar SEEDING performance, but the formulation was unstable over time.

Electrochemical setup and measurements

540 All the electrochemical processes and measurements were conducted in a

541 potentiostat-galvanostat EC-Lab (VSP model with a low-current option, BioLogic, France)

542 using a three-electrode configuration, with an external platinum wire as the counter

543 electrode and a miniaturised leak-free Ag/AgCl electrode as the reference electrode (cat#

544 ET072-1, Qrins). We used either photolithographic circular gold electrodes (Φ = 0.45 mm)

545   or gold rod electrodes (Φ = 2 mm) for the working electrodes, with in-house-built

546   connector boxes. For photolithographic electrodes, we attached laser-cut double-sided

547   adhesive tape (DFM 200 clear 150 POLY H-9 V-95, FLEXcon) with a rectangular shape

548   and a main channel in the centre to generate a 5–10 µL reservoir for incubation of

549   samples on the electrodes. For gold rod electrodes, we used the bottom of a tube as

550   electrochemical cell (cat# CLS430828-500EA, Sigma-Aldrich).

551   <u>Calculation diffusion of species</u>

552   The distance that electroactive diffusing particles moved away in one dimension from

553   the surface of the electrode after a certain time, that is, the thickness of the diffusion layer,

554   could be calculated using the root-mean-square displacement equation[35]:

$$\delta = \sqrt{2Dt} \tag{2}$$

556   where D (cm^2 s^{-1}) is the diffusion constant of the reacting species, and t is the time

557   (s). Using the parameters D = 9.0×10^{-6} cm^2 s^{-1} [36] and t = 0.001 s, the maximum diffusion

558   layer thickness was estimated as 1.9 µm.

559   The aggregation number of a micelle, N_{agg}, could be estimated[37]. The volume of the

560   hydrophobic tail is given by:

$$V_0 = 27.4 + 26.9n_c \ \text{Å}^3 \tag{3}$$

562   With n being the number of carbon atoms in the tail.

563   The radius of a micelle, with n_c carbon atoms in the long apolar tail of its monomers

564   and n_c' carbon atoms inside the chains could be approximated by:

$$R = 1.6 + 1.265(n_c + 1) + 0.421n_c' \ \text{Å} \tag{4}$$

566   Thus, with the volume of $^+N(CH_3)_3$ being 170 Å^3:

$$N_{agg} = \frac{^4/_3\pi R^3}{170 + V_0} \tag{5}$$

568   For CTA$^+$ we have $n_c = 16$, $n_c' = 1$, such that the radius is R = 23.5 Å and the $N_{agg} =$

569   87. However, considering the concentration of the electrolyte [NaCl] = 0.2 M, we could

570   estimate a N_{agg} of ~200, which is also in agreement with findings of other studies ($N_{agg} =$

571   75–170)[38].

572   In this scenario, we could estimate the diffusion constant D (m^2 s^{-1}) of a CTA$^+$ micelle

573   using the Stoke-Einstein equation:

$$D = \frac{k_B T}{6\pi\eta R_0} \tag{6}$$

575   where k_B is the Boltzmann constant (1.38065 × 10^{-23} m^2 kg s^{-2} K^{-1}), T is the

576   temperature (K), η is the viscosity of the medium (Pa s = kg m^{-1} s^{-1}), and R_0 is the radius

577   (m). Considering R_0 = 23.5 × 10^{-9} m, T = 298 K, and = 0.00089 Kg m^{-1} s^{-1}, we obtain D =

578   1.0 × 10^{-6} cm^2 s^{-1}. This diffusion constant is lower than that for free $AuCl_4^-$; thus, the quick

579   formation of $AuCl_4^-$-CTA micellar complexes diffuses ~2% of the distance from their free

580   counterpart, favouring the reutilisation of etched gold in the SEEDING process.

581   <u>SEEDING on photolithographic electrodes by step chronoamperometry</u>

582   SEEDING on photolithographic gold electrode chips conducted in 10 µL of SEEDING

583   solution, by step chronoamperometry, consisting of 20,000 cycles of step voltages, first

584   1.2 V for 1 ms and then -1.2 V for 2 ms. Finally, a chronoamperometric step at -1.2 V was

585   applied for 10 s to reduce gold oxides.

586   <u>SEEDING on rod electrodes by cyclic voltammetry</u>

587   SEEDING on rod electrodes was conducted in 5 mL of SEEDING solution, by cyclic

588   voltammetry, consisting of 20 cycles between 1.25 V and 0 V, starting at 0 V and a scan

589   rate of 0.1 V s^{-1}. Finally, a chronoamperometric step at -0.45 V was applied for 10 s to

590   reduce gold oxides.

591   Characterisation of electrochemical surface area

592   Electrodes were scanned by CV from 0 V to 1.6-1.8 V in an acidic solution of H_2SO_4

593   0.5 M at a scan rate of 0.1 V s^{-1}, integrating the area (charge) under the reduction curve

594   at ~0.9 V. The cathodic peak was proportional to the amount of gold being reduced;

595   therefore, it was proportional to the surface area. Assuming a specific charge transfer of

596   400 μC cm^{-2} [39, 40], it is possible to calculate the electrode area. By comparing it with the

597   geometric area we obtained the roughness factor.

598   Surface and topography characterisation by SEM and AFM

599   The topographic characterisation of the electrode surfaces was conducted using SEM

600   (S-4800, Hitachi High-Technologies) and AFM (DI-3100, Veeco). Before SEM

601   characterisation, the samples were sputter-coated with a 5 nm layer of gold (E-1045,

602   Hitachi). Imaging was performed at a 3–4 mm working distance at an accelerating voltage

603   of 7 kV. The NSG electrode roughness and morphology were characterised by AFM in

604   non-contact tapping mode using silicon AFM tips with a radius curvature <10 nm and

605   aluminium reflex coating (300AL-G-10, Woomyoung Inc.).

606   Contact angle measurements

607   Surface energy analysis was performed by water contact angle measurements, we

608   drop-casted 1 μL drops of water on different surfaces, and images were immediately

609   recorded. The images were analysed with ImageJ 1.53e, approximating the shape of the

610   profile droplets to a sphere using a seven-point manual selection procedure. The contact

611   angle was calculated using the following formula:

612
$$\theta = 2 \cdot \operatorname{atan}\left(\frac{2h}{l}\right) \tag{9}$$

613   where θ is the contact angle (rad), "h" is the height of the droplet, and "l" is the length

614   of the base of the drop.

615   <u>Crystallite size from X-ray diffraction</u>

616   NSG surfaces were prepared on diced chips (1 cm × 1.5 cm) with evaporated Ti/Au

617   (20/400 nm) on a glass wafer. An adhesive tape with a squared 4 mm side opening was

618   attached to the surface to generate a working electrode and cover the rest. The SEEDING

619   process was conducted following the same method used for the electrode chips (see

620   SEEDING on photolithographic electrodes by step chronoamperometry).

621   The samples were analysed by grazing incidence X-ray diffraction (XRD) (Bruker D8

622   Discovery) with a Cu K$\alpha_{(1+2)}$ radiation source, using an incident angle ω = 1º, and a

623   goniometer with 2θ range of 30°–80°.

624   The crystallite size was calculated from XRD spectra, fitting the peaks to a Gaussian

625   model with Fityk 1.3.1, using the full width at half maximum from peak Au(220), and using

626   the Scherrer equation:

627
$$\tau = \frac{K\lambda}{\beta cos\theta}$$

628   where τ is the mean size of the crystalline domain, K is the dimensionless shape

629   factor (0.94), λ is the X-ray wavelength (λ = 1.5418 Å), β is the line broadening (rad), and

630   θ is the Bragg angle (°).

631   <u>Electrochemical characterisation of gold crystalline faces</u>

632   We used SEEDING on photolithographic gold electrodes but using different oxidation

633   voltages, namely 1.20 V, 1.25 V, and 1.3 V. An additional set of electrodes was prepared

634   at 1.3 V, but the reduction step for 10 s at -1.2 V was omitted. Formation of different

635   crystalline gold faces generated on NSG electrodes was characterised electrochemically

636   in an acidic media of H_2SO_4 0.5 M by squared wave voltammetry, scanning from 0 V to

637   1.3 V at a scan rate of 0.02 V s^{-1} (pulse height 30 mV, pulse width 100 ms, step height 4

638   mV).

639   <u>Biofouling behaviour on NSG electrodes</u>

640   The biofouling behaviour of NSG surfaces was characterised by Faradaic

641   electrochemical impedance spectroscopy in two different media, BSA 1% or human

642   plasma, containing an equimolar concentration of ferrocyanide $K_4Fe(CN)_6$ and

643   ferricyanide $K_3Fe(CN)_6$ 2.5 mM. Measurements were performed from 0.1 MHz to 0.1 Hz,

644   at an amplitude of 5 mV *vs*. an open circuit potential. The R_{ct} of the NSG electrodes was

645   determined by fitting the data from Nyquist plots to a Randles equivalent circuit, in which

646   the R_S models the resistance of the solution; the constant phase element (non-ideal

647   capacitance) was used to model the double-layer capacitance (C_{dl}), and, in parallel, the

648   R_{ct} and a Warburg element (Z_W) modelled the diffusion of electroactive species in solution

649   (**Supplementary Fig. 5**).

650   <u>Electrochemical detection of redox molecules</u>

651   Electrochemical detection of ferro/ferricyanide at different concentrations (50, 25, 5,

652   2.5, 0.5, 0.25, 0.05, 0.025, 0.005, 0.0025 and 0 mM) was conducted on NSG electrodes

653   using squared wave voltammetry between 0 V and 0.6 V at a scan rate of 0.02 V s^{-1} (pulse

654   height 30 mV, pulse width 100 ms, step height 4 mV) using flat gold electrode as a control.

655   <u>Electrode functionalisation with capture antibodies</u>

656   The electrode chips were immersed in a fresh solution of L-cysteine 10 mM for 24 h

657   under constant shaking, and rinsed in ultrapure water. A glutaraldehyde solution 2.5%

658   prepared in PBS pH= 8 was drop-casted on the surface of the chips and incubated for 30

659 min, after which the chips were rinsed and dried. A 20 µg mL^{-1} of anti-IL6 solution (Thermo

660 Fisher Scientific, cat# CHC1263, lot# 172402) or anti-CD9 (BD Pharmingen, cat# 555370,

661 lot# 9014503) was prepared in PBS, and deposited on individual electrodes with a

662 hollowed ceramic needle (Φ_i = 350 µm; LabNEXT, Inc., no. 007-350) and incubated

663 overnight at 4 °C in a water-saturated atmosphere. After incubation, the electrodes were

664 washed with PBS Tween 20 0.05% in a shaker for 30 min to remove unbound antibodies.

665 Then, 10 µL of 1 M ethanolamine (Sigma-Aldrich, cat# E9508) in PBS, adjusted to pH 7.4,

666 with HCl, was drop-cast on each electrode and incubated at room temperature for 30 min

667 to neutralise the unreacted moieties. Finally, the chips were incubated in 1% BSA at room

668 temperature for 1 h before use.

669 <u>Cell culture of LNCaP cancer cells, EV isolation, and concentration</u>

670 The EVs for standards were extracted from LNCaP cell supernatant and enriched by

671 centrifugal force filtration inside a disc containing a 20 nm anodised aluminium oxide

672 membrane filter[41]. LNCaP cells were obtained from ATCC and cultured in Roswell Park

673 Memorial Institute medium (Gibco, Thermo Fisher Scientific) supplemented with 5% Exo-

674 Free FBS (Systems Biosciences, Inc.) and 1% antibiotics/antimycotics. The cells were

675 incubated at 37 °C with 5% CO_2 for 48 h. The cell culture supernatant was collected,

676 centrifuged at 300× g for 10 min, and centrifuged at 2000× g for 15 min to completely

677 remove dead cells and cellular debris. The supernatant was filtered through a 450 nm

678 filter.

679 <u>Preparation of EV standards</u>

680 Enriched EVs from LNCaP cells were used to prepare standards. EVs were

681 reconstituted in PBS to measure the particle count number by nanoparticle-tracking

682 analysis (Nanosight NS500, Malvern Instruments) and spiked in PBS or human plasma

683 samples at different dilution rates to prepare the calibration curves.

684   <u>Clinical samples</u>

685   The biospecimens and data from cancer patients used for this study were provided

686 by the Biobank of Pusan National University Hospital, a member of the Korea Biobank

687 Network. The study protocol was reviewed and approved by the IRB of Pusan National

688 University Hospital (IRB 1802-004-063). Plasma samples from healthy donors were

689 obtained from volunteers at the Yeungnam University Medical Center (IRB 2018-04-011).

690 The biospecimens were collected after written informed consent was received from all

691 subjects. Within 2 h of sample collection, urine was centrifuged at 500× g for 10 min at

692 4 °C to remove cellular debris and stored at −80 °C until analysis. Urine samples were

693 thawed for analysis and centrifuged at 2500× g for 15 min at 4 °C, and the precipitated

694 pellet was discarded. Blood samples, 3 mL, each were collected in vacutainer EDTA

695 collection tubes and processed within 2 h of collection. Samples were centrifuged at 300×

696 g for 10 min, 2000× g for 10 min at 4 °C to remove cells and debris, and stored at −80 °C

697 before use.

698   <u>Electrochemical enzymatic sandwich detection using NSG electrodes</u>

699   The reagents and dilutions used for the IL6 detection assay, and the washing steps,

700 were all conducted in assay buffer (1% BSA and 0.05% Tween 20 in PBS). IL6 (Thermo

701 Fisher Scientific, cat# CHC1263) was spiked at different concentrations in PBS and

702 human plasma, and 20 µL was incubated on the electrode chips for 2 h. The biotinylated

703 anti-IL6 detection antibody (Thermo Fisher Scientific, cat# CHC1263) was diluted to 1 µg

704 mL^{-1} and incubated on the chips for 1 h. To complete the assay, horseradish peroxidase

705 (HRP)-streptavidin (Thermo Fisher Scientific, cat# CHC1263) was diluted 1:400 in assay

706 buffer and incubated for 30 min. Enhanced One-Component HRP Membrane Substrate

707 (Sigma-Aldrich, cat# T9455) was incubated on the chips for 1 min. After each of the

708 previously described steps, the electrode chips were washed in a shacking Petri dish with

709 assay buffer for 15 min. The electrode chips were individually interrogated by cyclic

710 voltammetry at a scan rate of 0.1 V s^{-1} between -0.5 and 0.5 V $vs.$ open circuit potential

711 using the internal counter and pseudo-reference electrode of the chips. Other calibration

712 curves were obtained under different conditions by spiking IL6 in PBS instead of plasma

713 and using flat lithographic gold electrode chips for comparison.

714   The same assay was used to detect EVs in cell culture media and plasma using CD9

715 capturing antibodies and biotinylated CD9 (Abcam, monoclonal, clone# MEM-61, cat#

716 ab28094, lot# GR280437-1) at 1 µg mL^{-1}, biotinylated CD81 (LSBio, cat# LS-C134650,

717 clone# 1.3.3.22) at 1 µg mL^{-1} or biotinylated EpCAM (R&D Systems, cat# DY960, lot#

718 1336382) at 1 µg mL^{-1} as detection antibodies. Tween 20 was removed from the assay

719 entirely to prevent disruption of the lipid membrane of EVs during the assays. The

720 standards were prepared by diluting concentrated EV samples extracted from LNCaP cell

721 culture supernatant or spiked into human plasma at different dilutions.

722   Clinical urine and plasma samples from healthy and prostate cancer patient donors

723 were analysed in the same way by directly incubating the samples on the chips without

724 any pretreatment.

725 <u>Enzyme-linked immunosorbent assay</u>

726   ELISAs were conducted in 96-well plates (cat# 3364, Corning). All the volumes are

727 per well, washing twice with 200 µL of 0.1% BSA in PBS after each step. First, 50 µL of

728 anti-CD9 antibody (BD Biosciences, cat# 555370, clone M-L13) at 4 μg mL^{-1} was

729 incubated overnight at 4 °C. After blocking with 200 μL of 1% BSA for 3 h, 50 μL of sample

730 was incubated for 2 h. Then, 50 μL of biotinylated anti-CD9 (Abcam, cat# ab28094) or

731 anti-EpCAM (R&D systems, cat# DY960) at 500 ng mL^{-1} was incubated for 1 h. Finally,

732 50 μL of (HRP)-streptavidin (diluted 1:500 in 0.1% BSA) was incubated for 30 min.

733 Following addition of 50 μL of stop solution, the absorbance was measured at 450 nm

734 (Infinite 200 PRO NanoQuant Microplate Readers from Tecan, Tecan).

735   Statistical analysis

736   Statistical analysis was performed with Prism 9.1.0 (GraphPad). An α = 0.05

737 (confidence level 95%) was considered to be statistically significance, with *p*-values

738 *$p<0.05$, **$p<0.01$, ***$p<0.001$, and ****$p<0.0001$, respectively. The data presented in **Fig.**

739 **4e**, **Fig. 4f**, and **Supplementary Fig. 4b** were analysed by a two-tailed unpaired

740 parametric Welch's t-test (equal variance not assumed). ROC curves (**Fig. 4g** and

741 **Supplementary Fig. 4c**) were constructed using the Wilson/Brown method to calculate

742 the confidence interval[42].

743   Data availability

744   The data that support the plots within this paper and other findings of this study are

745 available from the authors upon reasonable request.

746 # Methods References

747 35.   Bard, A. & Faulkner, L. *Electrochemical Methods: Fundamentals and Applications*. (John
748   Wiley & Sons, Inc., New Jersey, 2001).
749
750 36.   Martín, H.*, et al.* Growth mode transition involving a potential-dependent isotropic to
751   anisotropic surface atom diffusion change. Gold electrodeposition on HOPG followed by
752   STM. *Langmuir.* **13**, 100-110 (1997).
753

754   37.   Roelants, E. & De Schryver, F. C. Parameters affecting aqueous micelles of CTAC, TTAC,
755   and DTAC probed by fluorescence quenching. *Langmuir.* **3**, 209-214 (1987).
756

757   38.   Haynes, W. M. *CRC Handbook of Chemistry and Physics*, vol. 96. (CRC Press, California,
758   2016).
759

760   39.   Hoogvliet, J. C., Dijksma, M., Kamp, B. & van Bennekom, W. P. Electrochemical
761   pretreatment of polycrystalline gold electrodes to produce a reproducible surface
762   roughness for self-assembly: A study in phosphate buffer pH 7.4. *Anal. Chem.* **72**, 2016-
763   2021 (2000).
764

765   40.   Cherevko, S., Topalov, A. A., Zeradjanin, A. R., Katsounaros, I. & Mayrhofer, K. J. J. Gold
766   dissolution: towards understanding of noble metal corrosion. *RSC Advances.* **3**, 16516-
767   16527 (2013).
768

769   41.   Woo, H.-K.*, et al.* Urine-based liquid biopsy: non-invasive and sensitive AR-V7 detection
770   in urinary EVs from patients with prostate cancer. *Lab. Chip.* **19**, 87-97 (2019).
771

772   42.   Brown, L. D., Cai, T. T. & DasGupta, A. Interval estimation for a binomial proportion. *Stat.*
773   *Sci.* **16**, 101-133, 133 (2001).
774
775

Acknowledgements

Author contributions

Conception and experimental design were performed by J.S.R. and Y.-K.C. Experiments, data analyses, validation, and reproducibility were conducted by J.S.R. ELISA assays were performed by H.-K.W. J.-H.P. conducted cell cultures and clinical sample handling and storage. The biospecimens and corresponding data of prostate cancer patients were

791 **Competing interests**

793 **Additional information**

Supplementary Files

This is a list of supplementary files associated with this preprint. Click to download.

- 20211008SI.pdf